

Single-Step Deposition of Cerium-Substituted Yttrium Iron Garnet for Monolithic On-Chip Optical Isolation

Xue Yin Sun,*^{†,‡} Qingyang Du,[†] Taichi Goto,[§] Mehmet C. Onbasli,[†] Dong Hun Kim,[†] Nicolas M. Aimon,[†] Juejun Hu,[†] and Caroline A. Ross*,[†]

[†]Department of Materials Science and Engineering, Massachusetts Institute of Technology, Cambridge, Massachusetts 02139, United States

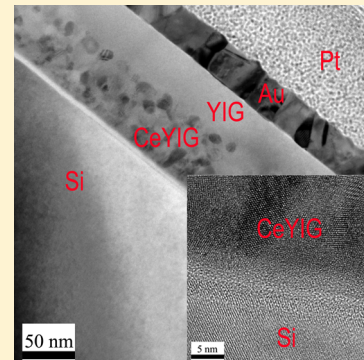
[‡]School of Materials Science and Engineering, Harbin Institute of Technology, Harbin 150001, PR China

[§]Toyohashi University of Technology, Hibarigaoka, Tempaku, Toyohashi, Aichi 441-8580, Japan

Supporting Information

ABSTRACT: Photonic integrated circuits require magneto-optical (MO) materials for making nonreciprocal devices such as isolators and circulators. The most successful MO materials are rare-earth-substituted iron garnets, but these can be challenging to grow on silicon without a seed layer, which introduces spacing loss between the waveguide and the MO cladding. A pulsed-laser deposition (PLD) method is used for making MO Ce:YIG ($\text{Ce}_1\text{Y}_2\text{Fe}_5\text{O}_{12}$)/YIG ($\text{Y}_3\text{Fe}_5\text{O}_{12}$) bilayer or trilayer films on different substrates, including silicon, quartz, and $\text{Gd}_3\text{Ga}_5\text{O}_{12}$ (GGG), in which a multilayer film is deposited in one run and then annealed. A YIG seed layer grown above the MO Ce:YIG facilitates recrystallization during ex situ rapid thermal annealing, which results in a reduced thermal budget and simplified deposition process. A monolithically integrated optical isolator was demonstrated by direct deposition of a bilayer Ce:YIG/YIG capping layer onto a silicon-on-insulator resonator. The device exhibited an insertion loss of 7.4 ± 1.8 dB and an isolation ratio of 13.0 ± 2.2 dB within the telecommunication window ($\lambda = 1564.4$ nm), which outperforms previously reported monolithic isolators.

KEYWORDS: optical isolator, magneto-optical, cerium iron garnet, pulsed-laser deposition, monolithic integration, magneto-optical garnet



Optical isolators are nonreciprocal photonic devices that allow light propagation in only one direction. By breaking time-reversal symmetry, degeneracy of forward and backward propagating photonic modes is lifted, enabling nonreciprocal wave propagation.^{1,2} Time-reversal symmetry is typically broken using magneto-optical (MO) materials whose permittivity tensor has nonvanishing off-diagonal components, such as yttrium iron garnet (YIG, $\text{Y}_3\text{Fe}_5\text{O}_{12}$) and cerium-doped YIG (Ce:YIG, $\text{Ce}_1\text{Y}_2\text{Fe}_5\text{O}_{12}$).^{3–5} In particular, Ce:YIG is considered to be a promising isolator material for 1550 nm wavelength given its large MO figure of merit, defined as Faraday rotation divided by optical absorption, and on-chip optical isolators made out of Ce:YIG have been demonstrated by several groups.^{6–11} Although these demonstrations represent an important step toward on-chip optical isolation, it is mandatory that both MO material/device integration technology and MO film quality (in terms of MO figure of merit, FOM) are further improved to fulfill the demanding requirements of photonic integration.

On-chip integration of YIG-based materials has been challenging because they cannot be grown heteroepitaxially on classical semiconductor substrates. This is because of the large thermal budget required for garnet growth as well as lattice and thermal expansion coefficient mismatch between

garnets and common semiconductors. YIG and Ce:YIG films have complex cubic unit cells with lattice parameters (YIG: 12.376 Å) much larger than those of Si ($a = 5.431$ Å), GaAs ($a = 5.6533$ Å), and InP ($a = 5.8696$ Å).^{12–14} The coefficient of thermal expansion (CTE) for garnet films is much larger than that for most semiconductors as well (YIG: 10.4×10^{-6} K⁻¹, Si: 3×10^{-6} K⁻¹, and GaAs and InP: 5×10^{-6} K⁻¹).¹⁵ Because of the large CTE mismatch, a low growth temperature is desired in order to prevent garnet film cracking. A reduced thermal budget is also critical to on-chip device integration. YIG and substituted garnet films have been integrated on photonic substrates using wafer bonding,⁹ metal–organic chemical vapor deposition (MOCVD),¹⁶ sputtering,^{17–26} and pulsed-laser deposition (PLD).^{3–7,27–30} Wafer bonding capitalizes on the excellent MO properties of single-crystal bulk garnet; nevertheless, this hybrid integration approach adds to processing complexity. The other methods allow monolithic integration of garnets on semiconductors, although the resulting films suffer from reduced MO FOM compared to bulk garnet. A two-step PLD process was demonstrated in which a thin YIG buffer layer was grown then crystallized by rapid thermal annealing (RTA)

Received: January 26, 2015

Published: June 10, 2015



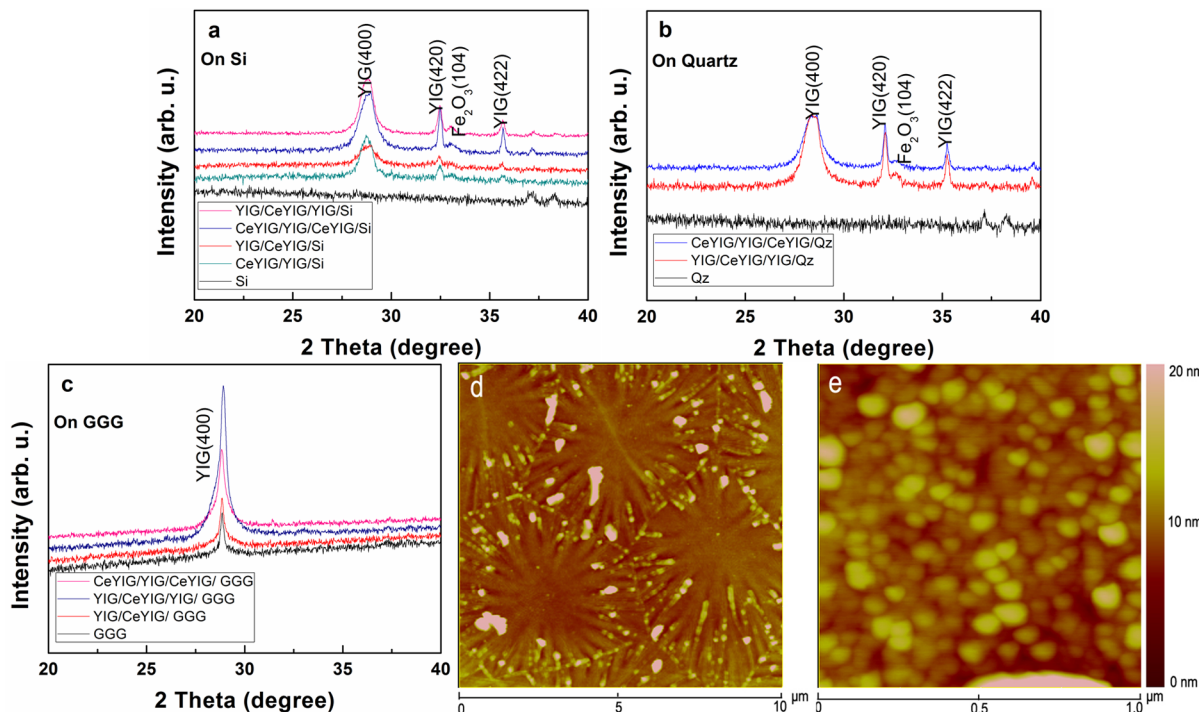


Figure 1. XRD results and AFM images of the films on different substrates after RTA. 1D XRD ω - 2θ scans for the films on (a) silicon and (b) quartz, including scans of bare substrates for comparison. (c) 1D XRD ω - 2θ scans for the films on single crystal GGG (100) substrates. AFM images of (d) YIG/CeYIG/Si, $10 \mu\text{m} \times 10 \mu\text{m}$ area, and (e) CeYIG/YIG/Si, $1 \mu\text{m} \times 1 \mu\text{m}$ area.

for 5 min, serving as a seed layer for subsequent growth of polycrystalline Ce:YIG on Si and silica.^{4,6} On silicon nitride, slow growth of the YIG seed layer improved the magnetic properties and Faraday rotation of Ce:YIG grown on top of it.⁷ Films have also been produced by sputtering using a similar two-step process in which a YIG layer was grown, annealed, and used as a seed layer for Ce:YIG or Bi:YIG growth.²⁵

In this work, we demonstrate a PLD method for making Ce:YIG films on a variety of substrates in which a YIG layer acts as an in situ seed layer for Ce:YIG during the crystallization of both YIG and Ce:YIG. Layers of both YIG and Ce:YIG are deposited in one step followed by an anneal. Crystallization of the Ce:YIG during RTA is facilitated by YIG layer(s) on top of or at the bottom of the stack. This simplifies the process flow because only one deposition step is required instead of two and leads to films with good magnetic and MO properties. The finding that a YIG overlayer can promote Ce:YIG crystallization as well as a conventional YIG underlayer enables Ce:YIG to be grown directly on a waveguide, maximizing its interaction with the guided light without the spacing loss caused by a weakly magneto-optical YIG underlayer. The one-step deposited garnet films grown on silicon have very high optical and MO quality. A resonator isolator device is used as a test vehicle to demonstrate the optical properties of the garnet. This growth method is applicable to other nonreciprocal integrated photonic devices.

Ce:YIG and YIG films with layer structures consisting of YIG 30 nm/Ce:YIG 60 nm/substrate and Ce:YIG 60 nm/YIG 30 nm/substrate (with a total thickness of 90 nm) and trilayers YIG 30 nm/Ce:YIG 140 nm/YIG 30 nm and Ce:YIG 70 nm/YIG 60 nm/Ce:YIG 70 nm (with a total thickness of 200 nm) were deposited on (001) silicon (Si) and Z-cut (0001) quartz (Qz) using PLD, followed by annealing. Identical layer sequences were also grown on (100) GGG substrates as references.

Figure 1 shows the XRD diffraction data for the bilayers and trilayers after RTA²¹ at 800 °C for 5 min. The YIG (400) peak exhibits the highest intensity in all samples on Si and Qz as shown in Figure 1a,b, which indicates that the film has a preferred (100) texture based on that of the Powder Diffraction File, in which (420) has the highest intensity. In contrast, the XRD results for the films grown on GGG after RTA are shown in Figure 1c, indicating an epitaxial single-crystal film for all layer sequences with no secondary phases. Garnet films grown and crystallized on Si and quartz are polycrystalline because there is no epitaxial relationship with the substrate. As a result, YIG (420) and (422) peaks are observed in addition to the major YIG (400) peak in Figure 1a,b. However, the garnet films on GGG (100) are lattice-matched and single-crystal, and the diffraction pattern shows YIG (*h*00) peaks near the GGG (*h*00) substrate peaks.

The out-of-plane (OP) lattice constant of the films was 12.39 Å, similar to that reported for YIG films (12.38 Å).⁴ The weak peak at $33.1 \pm 0.05^\circ$ for films on Si and Qz was attributed to hematite, $\alpha\text{-Fe}_2\text{O}_3$,⁶ an antiferromagnet.

The AFM surface morphology of the bilayer films on Si is shown in Figure 1d,e. For the YIG/Ce:YIG/Si, the grain size at the top surface was up to 5 μm , and the grains showed a radiating pattern, whereas in Ce:YIG/YIG/Si, dense topographic features up to ~ 50 nm across were visible. In comparison, Ce:YIG films grown on a YIG seed layer on Si_3N_4 using the two-step deposition process also showed grains with a radiating pattern at least a few micrometers across,⁷ and large grains have also been seen in single-layer YIG grown on other substrates such as diamond (unpublished).

Figure 2 presents transmission electron microscopy (TEM) and elemental mapping images of YIG (30 nm)/CeYIG (60 nm)/Si (Figure 2a,c,e) and YIG (30 nm)/CeYIG (60 nm)/YIG (30 nm)/Si (Figure 2b,d,f). In both samples, the grain size in

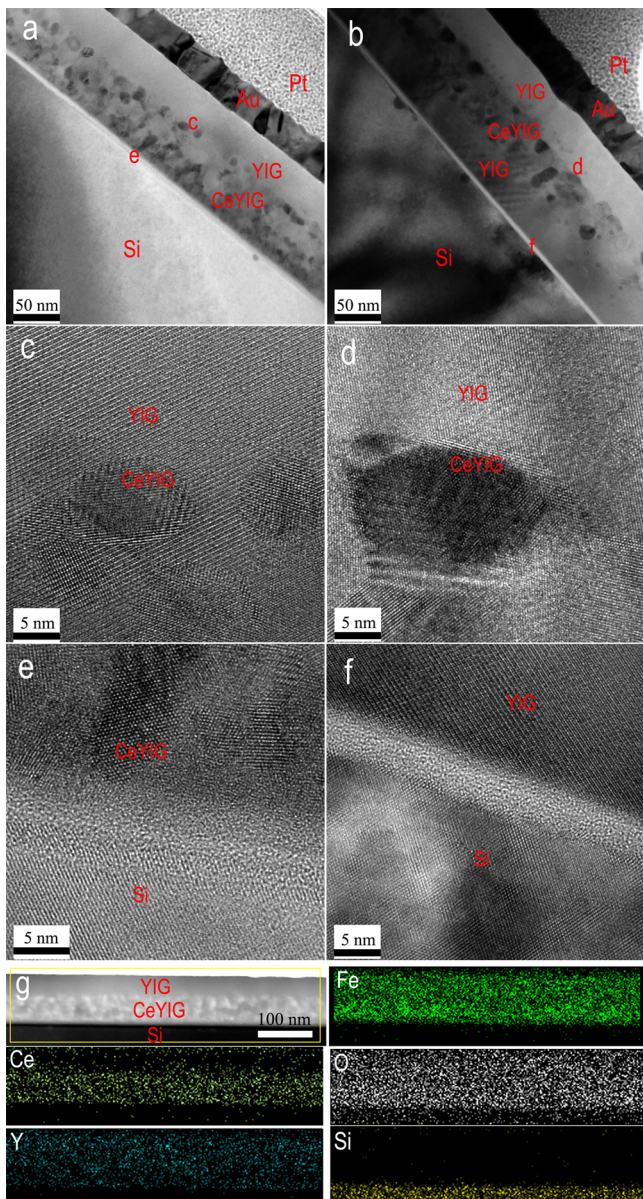


Figure 2. TEM images and element mapping of films on Si. (a, c, and e) YIG/CeYIG/Si and (b, d, and f) YIG/CeYIG/YIG/Si (YIG 30 nm, CeYIG 60 nm). (a and b) Bright-field TEM cross-sectional images. (c and d) HRTEM images of the interface between the YIG and Ce:YIG layer. (Location observed was marked in Figure 2a as “c” and Figure 2b as “d”, respectively.) (e and f) HRTEM images of the interface between the substrate (Si) and the films. (Location observed was marked in Figure 2a as “e” and in Figure 2b as “f”.) (g) STEM image and STEM-EDX element mappings of the YIG/CeYIG/Si film show the layer structure qualitatively.

the Ce:YIG layer was less than 20 nm, but the YIG layer consisted of much larger grains, larger than the field of view in Figure 2a,b. High-resolution (HR) TEM images of the interface between the YIG layer and the Ce:YIG layer are shown in Figure 2c,d. The orientation of the large YIG grains was (100), whereas the orientations of the small grains in the Ce:YIG layer varied. Figure 2e shows HRTEM images of the interface between film and substrate (silicon with native oxide) for YIG/Ce:YIG/Si. The Ce:YIG layer in contact with the amorphous SiO_x was crystalline, with a ~1 nm thick layer of amorphous Ce:YIG at the interface. In contrast, in YIG/Ce:YIG/YIG/Si,

the YIG in contact with the Si was a large fully crystallized grain with (100) orientation (Figure 2f). The element distribution map in Figure 2g of the YIG/CeYIG/Si illustrates uniform distribution of Y throughout the layers and localization of Ce in the Ce:YIG layer as anticipated. Fe, however, showed a less uniform distribution in the Ce:YIG layer than in the YIG.

Growing a Ce:YIG film and annealing under the same conditions did not yield garnet-structured films on nongarnet substrates. Prior work also showed that in the absence of the YIG layer crystallization of the Ce:YIG layer is impeded.^{4,6,23–25} The present results extend this result to show that the templating effect of YIG on Ce:YIG growth exists even if both layers are simultaneously crystallized. YIG is assumed to crystallize first, providing a large-grained layer that promotes crystallization of Ce:YIG, even if YIG is placed on top of the Ce:YIG.

Magnetic properties of Ce:YIG films were measured with magnetic fields applied in-plane (IP) with the film or perpendicular to the film plane (out-of-plane, OP) at room temperature using a vibrating sample magnetometer (VSM). The hysteresis loops at room temperature are given in Figure 3a–f. The saturation magnetization (M_s , averaged over all the garnet layers) of the films was 115 emu cm^{-3} (with ~5% error estimate) for the Ce:YIG/YIG/Si and 113 emu cm^{-3} for the YIG/CeYIG/Si (Figure 3a,b). The M_s of the three-layer films on Si was 103 emu cm^{-3} . The M_s of the films on Qz was about 108 emu cm^{-3} (Figure 3c,d). The M_s of the films on GGG after RTA was 110 emu cm^{-3} , as shown in Figure 3f, which is higher than the unannealed values (Figure 3e). These results are consistent with the samples being primarily garnet phase without significant magnetite or maghemite spinel phases. The IP coercivity, H_c , of annealed single-crystal multilayer films on GGG was <10 Oe, and it was below 100 Oe for films on Si and quartz. In Figure 3f, the slope in the tail of the YIG/Ce:YIG/GGG loop is due to noise from the substrate, which has a strong paramagnetic signal.

The bulk saturation magnetization at room temperature of YIG is about 140 emu cm^{-3} ,³¹ and for Ce:YIG, it is 118 emu cm^{-3} , slightly higher than that of the films made in this study.³² The seed layer deposition conditions, in particular deposition rate⁷ as well as the annealing temperature²⁶ have an important effect on the magnetic properties, for example, via their effect on oxygen content and cation ratios. Growth parameters were not explored in detail in the present study, and it is expected that the M_s could be increased by further optimization to be closer to bulk values.

The films all have high remanence IP with an OP hard axis, but the magnitude of the net anisotropy differs between the films grown on different substrates. The net anisotropy can be estimated from the hard axis (i.e., the OP) saturation field, H_K , which was 1400 Oe for films on Si and 3500 Oe for films on Qz. The anisotropy, K_{tot} , consists of the sum of shape anisotropy (producing $H_K = 4\pi M_s$, in cgs units), magneto-crystalline, and magnetoelastic contributions. For YIG, the shape anisotropy of 1.2×10^5 erg cm^{-3} is the dominant factor leading to $H_K = 1760$ Oe in unstrained polycrystalline YIG films with bulk M_s . The room-temperature magnetocrystalline anisotropy is small (~ 10^4 erg cm^{-3}), and the magnetostriction coefficient is small, $\lambda_{100} = -1.3 \times 10^{-6}$.³³ The magnetocrystalline anisotropy of Ce:YIG is not well-known, but will be neglected here because the polycrystallinity of the Ce:YIG layers resulting from the random orientations of the Ce:YIG grains averages out the net magnetocrystalline anisotropy of the

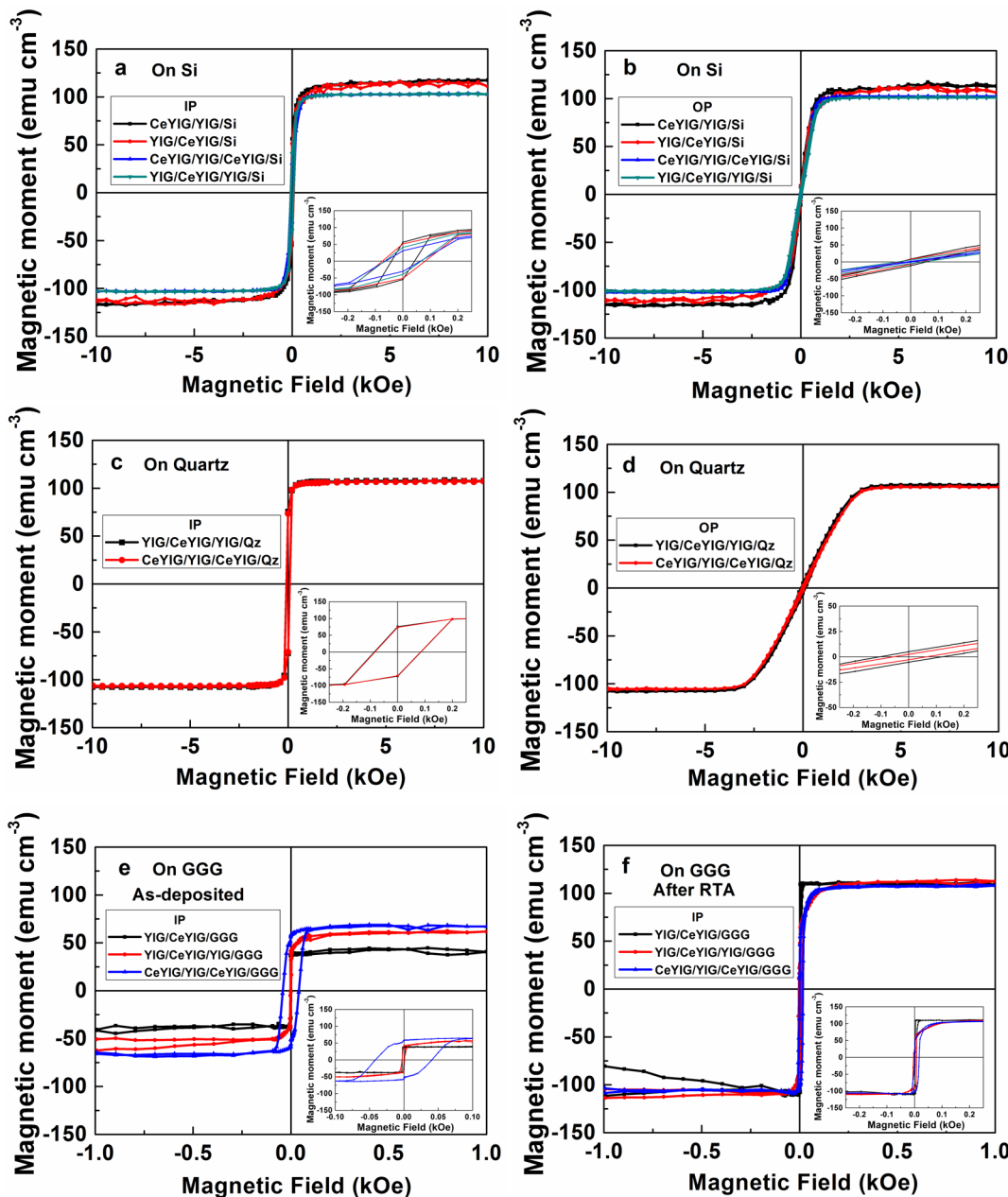


Figure 3. Magnetic properties of the films. (a) In-plane (IP) and (b) Out-of-plane (OP) hysteresis loops of films on Si after RTA. (c) IP and (d) OP hysteresis loops of films on quartz after RTA. IP hysteresis loops of films on the single crystal GGG (100) (e) before and (f) after RTA.

film. The room-temperature magnetostriction coefficient of $\text{Ce}_3\text{Fe}_5\text{O}_{12}$ (extrapolated from small concentrations of Ce) has been given as $\lambda_{100} = +120 \times 10^{-6}$ and $\lambda_{111} = +50 \times 10^{-6}$.³⁴ Data on $\text{Ce}_x\text{Y}_{1-x}\text{Fe}_5\text{O}_{12}$ in the range of $x = 0$ –0.125 also show that Ce contributed a positive magnetostriction,³⁵ suggesting that the $x = 1$ composition used here should have a positive magnetostriction. If we extrapolate from ref 35, then we obtain $\lambda_{100} \approx +10 \times 10^{-6}$ at $x = 1$, which is smaller than the value of extrapolation from ref 34. Considering that the Ce:YIG occupies only about half the volume of the film the effective magnetostriction of the film will be reduced from this value but is still expected to be positive. An estimate of the magnetoelastic anisotropy is $(^3/2)\lambda_{100}E\varepsilon_z$, where ε_z is the OP strain and E is Young's modulus, 200 GPa.³⁶ The IP thermal mismatch strain $\varepsilon_x = -\varepsilon_z/2$ is determined by the product of the difference in thermal expansion coefficients and the temper-

ature change. Garnet films on Si will experience tensile strain after cooling from 800 °C, with $\varepsilon_x \approx 6 \times 10^{-3}$ (neglecting temperature dependence of the thermal expansion coefficients), whereas for films on crystalline quartz with an IP thermal expansion coefficient of 13.7×10^{-6} , the films will experience compressive strain,^{37,38} $\varepsilon_x \approx -3 \times 10^{-3}$. These thermal mismatch strains, combined with the positive magnetostriction, would suggest that the films on Qz would be easier to magnetize in the OP direction than those on Si, but the OP saturation field, H_K , was higher for the films on Qz not lower. This suggests that the thermal mismatch may not be the only source of strain in the films, i.e., the films were not fully relaxed at the annealing temperature as strain developed during the crystallization process. It is also possible that the extrapolated magnetostriction parameters are not accurate for this composition.

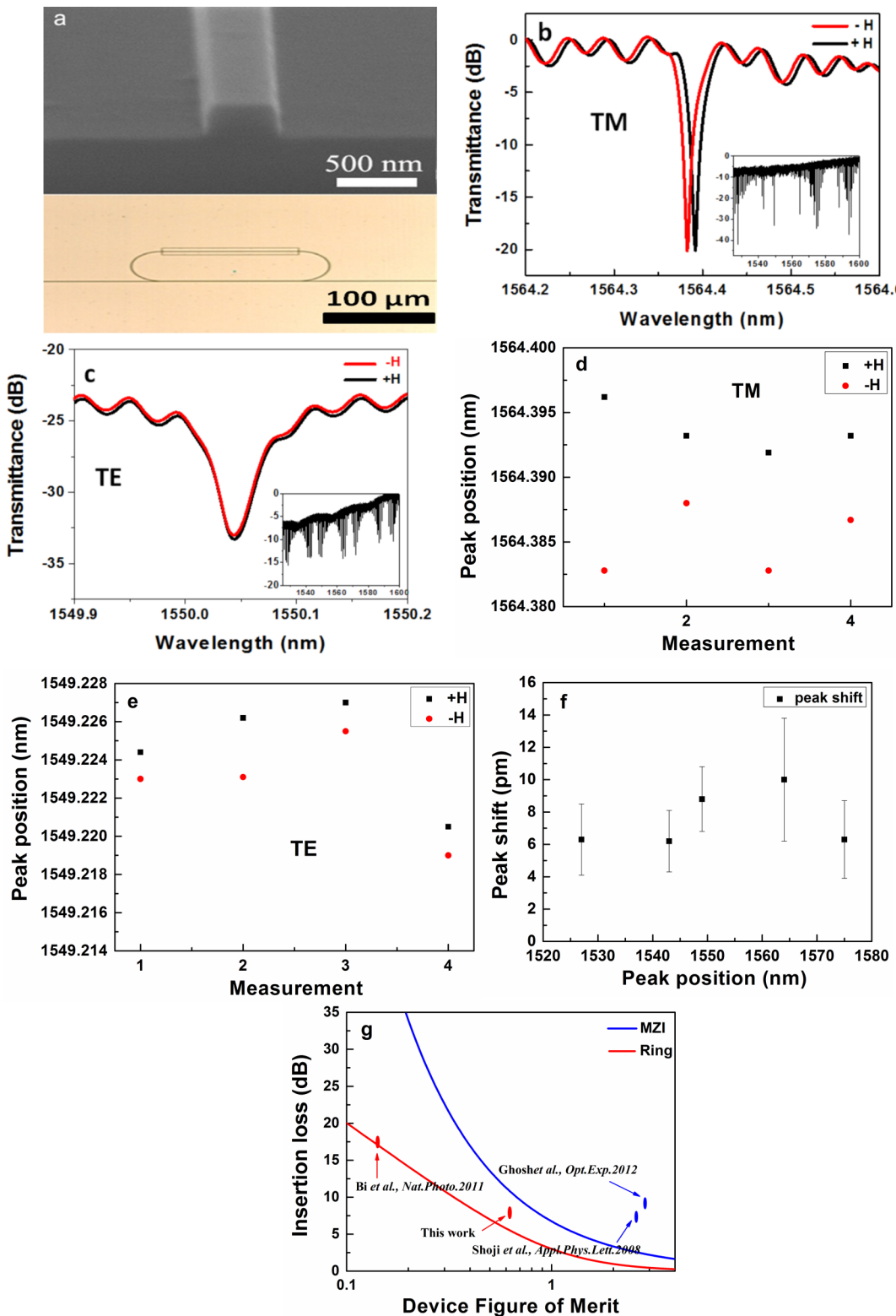


Figure 4. (a) Tilted-view SEM micrograph of the silicon-on-insulator waveguide (top) and an optical micrograph of the resonator (bottom). (b) Transmission spectra of TM mode under applied magnetic fields of opposite directions. Insertion loss measured from the figure is 7.4 dB. (c) Transmission spectra of TE mode under applied magnetic fields of opposite directions. (d) TM mode resonant peak positions measured when the magnetic field direction was reversed 8 consecutive times. (e) TE mode resonant peak positions measured when the magnetic field direction was reversed eight consecutive times. (f) Wavelength dependence of nonreciprocal resonant peak shift measured at several resonant peak locations. (g) Insertion losses of isolators. Solid lines are simulated performance of ideal microring and MZI devices, whereas the dots correspond to experimental measurement results in this report and literature.

To quantify the MO behavior of the films in an integrated device, we fabricated integrated optical isolator devices by depositing YIG (top layer, 30 nm) on CeYIG (bottom layer, 60 nm) films on top of silicon-on-insulator racetrack resonators. The resonator device serves as a test vehicle to validate the MO material and waveguide performance, which are otherwise difficult to measure. The film growth process can be readily transferred to other isolator designs such as Mach-Zehnder interferometers, which are capable of broadband operation.^{39–41} Figure 4a shows a tilted-view SEM micrograph of the silicon-on-insulator waveguide and a top view of the isolator, which consists of a racetrack resonator adjacent to a waveguide.⁴ The Q factor of the resonator without garnet was $\sim 3.4 \times 10^4$, and the free spectral range was ~ 0.82 nm. These values are similar to those in ref 4.

Prior to MO film deposition, the waveguide was coated with a 1 μm thick SiO_2 cladding, and a window was subsequently opened in the cladding layer via wet etching. Therefore, only the waveguide section in the window region is in direct contact with the MO film and is magneto-optically active. The total length of the racetrack resonator was 682 μm , and the oxide window was 200 μm in length. Details of the fabrication process are described in ref 24. Figure 4b,c plots the transmission spectra of quasi-transverse magnetic (TM) and quasi-transverse electric (TE) modes through the isolator, respectively, measured for positive and negative magnetic fields applied IP perpendicular to the garnet-clad section of the resonator. A resonant peak shift caused by nonreciprocal phase shift (NRPS) in the waveguide is clearly visible for the TM mode, whereas the TE mode exhibits negligible resonant peak shift, consistent with our magnetic field configuration. The device insertion loss is estimated to be 7.4 ± 1.8 dB, and the isolation ratio is 13 ± 2.2 dB according to the definition given in ref 4. The Faraday rotation of the Ce:YIG film was estimated to be $1100^\circ \text{ cm}^{-1}$ using perturbation theory.⁴

The resonant wavelengths obtained from the measurements are plotted in Figure 4d,e. The average peak shift from four separate measurements is 9.6 ± 4.1 pm for the TM mode and 1.7 ± 0.4 pm for the TE mode. The small drift over repeated measurements at room temperature is likely a result of temperature change (Experimental Methods). Figure 4f plots the wavelength dependence of the nonreciprocal resonance shift.

To benchmark the performance of our device, we simulated the insertion losses of ideal isolator devices that are based on microring resonator and Mach-Zehnder interferometer (MZI) geometries, respectively, using procedures detailed in the Supporting Information. We choose insertion loss rather than isolation ratio as the performance benchmark here because it is directly correlated with the MO FOM of the nonreciprocal device, defined as

$$\text{FOM} = \frac{\Delta\beta}{\alpha} \quad (1)$$

where $\Delta\beta$ denotes the nonreciprocal phase shift (NRPS), i.e., the propagation constant difference of forward and backward propagating modes in the waveguide, and α gives the waveguide loss. In contrast, isolation ratio is not an intrinsic parameter reflecting the MO FOM of the isolator devices because it can be maximized by approaching the critical coupling condition in microrings or by tuning the power-splitting ratio in two interferometer arms in the case of MZI.

The simulated insertion losses are plotted in Figure 4g as solid lines, and the points denote the device insertion loss demonstrated in this paper as well as values quoted from the literature.^{4,11,39} The significant improvement of our device performance compared to that of our earlier results is mainly attributed to reduced garnet material loss, and we anticipate that material processing improvement will further enhance the MO characteristics of deposited Ce:YIG films.

In conclusion, polycrystalline MO two- and three-layer garnet films were grown on Si and quartz substrates using a single-step PLD method in which Ce:YIG/YIG bilayers and trilayers were grown and then annealed. We found that YIG layers grown either above or below the Ce:YIG serve as effective seed layers to promote crystallization of the MO Ce:YIG layers. This avoids the need for a YIG layer between the waveguide and the Ce:YIG. Growth of the Ce:YIG directly in contact with the waveguide increases optical coupling into the Ce:YIG. The top-down crystallization of the Ce:YIG provides enhanced design options for nonreciprocal optical devices and may be applicable in other materials systems where a seed layer is needed to ensure correct phase formation in a functional layer. The films were compared to single-crystal films grown on GGG substrates and had similar magnetization. An integrated resonator optical isolator was fabricated on a Si waveguide and showed an insertion loss of 7.4 ± 1.8 dB and an isolation ratio of 13.0 ± 2.2 dB at 1564.4 nm wavelength, which represents significant performance improvement over previously demonstrated monolithic on-chip isolators.

EXPERIMENTAL METHODS

MO Film Growth. The films were deposited on (001) Si, (100) GGG, and Z-cut quartz (0001) substrates and silicon-on-insulator waveguides by PLD. The composition and fabrication process of YIG and Ce:YIG targets are the same as those in refs 4 and 6. The target was ablated by a KrF excimer laser at a wavelength of 248 nm, 10 Hz repetition rate, and a fluence of 2 J cm^{-2} . The substrate temperature was held at 650° C throughout the deposition. The distance between the substrate and the targets was 6 cm. The chamber was pumped to 5×10^{-6} Torr base pressure for PLD. During PLD for YIG and Ce:YIG growth, the oxygen pressure was maintained at 25 mTorr. After deposition, the samples were kept at 650° C for 15 min at 500 Torr oxygen pressure and then cooled to 200° C at a ramping rate of $5^\circ \text{ C min}^{-1}$ under 500 Torr oxygen pressure. The films were subsequently subjected to RTA (Modular Process Tech, RTP-600S) at 800° C for 5 min.

Materials Characterization. Phase identification and texture analysis were carried out using X-ray diffraction. Conventional $\theta-2\omega$ Bragg diffraction data were collected on a PANalytical X'pert Pro MPD diffractometer. The thickness was measured by surface profilometry on a KLA-Tencor P-16+ stylus profiler with a measurement error of less than 5%. Samples for TEM were prepared using focused ion beam (FEI-600) and then imaged on a JEOL 2010F field-emission TEM at 200 kV acceleration voltage. The element distribution in the sample was mapped by STEM EDX. Magnetic properties were characterized at room temperature by VSM using an ADE Technologies VSM Model 1660.

Device Fabrication and Testing. The optical isolator fabrication process is described in ref 24. The deposition parameters for YIG (30 nm)/CeYIG (60 nm) films on the optical isolator is same as that of the YIG (30 nm)/CeYIG (60 nm)/Si film. (The film was deposited in the same run along

with the TEM sample shown in Figure 2a.) After RTA, transmission spectra of the optical isolator was analyzed on a Newport Auto Align workstation coupled with an optical vector analyzer (LUNA Technologies OVA-5000). Near-infrared laser light was coupled in and out of the chip through tapered lens-tip fibers. During the measurement, a permanent magnet was placed by the side of sample to produce ~ 1000 Oe magnetic field IP and perpendicular to the racetrack waveguide section in the window region. Optical isolation performance of the device was tested by reversing the magnetic field direction while maintaining the same light propagation direction, which is equivalent to reversing the light propagation direction. To mitigate the effect of temperature fluctuations, which can lead to spurious resonance shift, the transmission measurement was repeated multiple times with the magnetic field directions reversed. The interval between each measurement is about 2 min. The temperature-dependent wavelength shift (TDWS) of the nonreciprocal resonator is about 57 pm/K. Our measurement setup temperature stability is ± 0.1 K. Consequently, we anticipate approximately ± 0.006 nm drift in the measured resonant wavelengths, which is consistent with the data shown in Figure 4.

ASSOCIATED CONTENT

Supporting Information

Derivation of the quantitative relation between the insertion losses of ideal microring and MZI isolators and the MO device figure of merit F_{res} . The Supporting Information is available free of charge on the ACS Publications website at DOI: 10.1021/acsphtnics.Sb00026.

AUTHOR INFORMATION

Corresponding Authors

*E-mail: hit2001sun@hit.edu.cn.

*E-mail: caross@mit.edu.

Notes

The authors declare no competing financial interest.

ACKNOWLEDGMENTS

This work was supported by the National Science Foundation under award no. ECCS-1231392, FAME, a STARnet Center of SRC sponsored by DARPA and MARCO, Japan Society for the Promotion of Science Grant-in-Aid for Young Scientists (A) no. 26706009, and Challenging Exploratory Research no. 26600043. A Fellowship from the Chinese Scholarship Council (CSC) is gratefully acknowledged. This work made use of the MRSEC Shared Experimental Facilities supported by the National Science Foundation under award no. DMR-1419807. We thank Jinshuo Zhang and Kun-Hua Tu for their assistance with experiments.

REFERENCES

- (1) Lira, H.; Yu, Z.; Fan, S.; Lipson, M. Electrically Driven Nonreciprocity Induced by Interband Photonic Transition on a Silicon Chip. *Phys. Rev. Lett.* **2012**, *109*, 033901.
- (2) Yang, Y.; Galland, C.; Liu, Y.; Tan, K.; Ding, R.; Li, Q.; Bergman, K.; Baehr-Jones, T.; Hochberg, M. Experimental demonstration of broadband Lorentz non-reciprocity in an integrable photonic architecture based on Mach-Zehnder modulators. *Opt. Express* **2014**, *22*, 17409–17422.
- (3) Bi, L.; Hu, J.; Ross, C. A. Fabrication and characterization of $\text{As}_2\text{S}_3/\text{Y}_3\text{Fe}_5\text{O}_{12}$ and $\text{Y}_3\text{Fe}_5\text{O}_{12}/\text{SOI}$ strip-loaded waveguides for integrated optical isolator applications. *Proc. SPIE* **2010**, *7604*, 760406.

(4) Bi, L.; Hu, J.; Jiang, P.; Kim, D. H.; Dionne, G. F.; Kimerling, L. C.; Ross, C. A. On-chip optical isolation in monolithically integrated non-reciprocal optical resonators. *Nat. Photonics* **2011**, *5*, 758–762.

(5) Bi, L.; Hu, J.; Dionne, G. F.; Kimerling, L. C.; Ross, C. A. Monolithic integration of chalcogenide glass/iron garnet waveguides and resonators for on-chip nonreciprocal photonic devices. *Proc. SPIE* **2011**, *7941*, 794105.

(6) Goto, T.; Onbasli, M. C.; Ross, C. A. Magneto-optical properties of cerium substituted yttrium iron garnet films with reduced thermal budget for monolithic photonic integrated circuits. *Opt. Express* **2012**, *20*, 28507–28517.

(7) Onbasli, M. C.; Goto, T.; Sun, X.; Huynh, N.; Ross, C. A. Integration of bulk-quality thin film magneto-optical cerium-doped yttrium iron garnet on silicon nitride photonic substrates. *Opt. Express* **2014**, *22*, 25183–25192.

(8) Mizumoto, T.; Takei, R.; Shoji, Y. Waveguide Optical Isolators for Integrated Optics. *IEEE J. Quantum Electron.* **2012**, *48*, 252–260.

(9) Tien, M.-C.; Mizumoto, T.; Pintus, P.; Kromer, H.; Bowers, J. E. Silicon ring isolators with bonded nonreciprocal magneto-optic garnets. *Opt. Express* **2011**, *19*, 11740–11745.

(10) Shoji, Y.; Ito, M.; Shirato, Y.; Mizumoto, T. MZI optical isolator with Si-wire waveguides by surface-activated direct bonding. *Opt. Express* **2012**, *20*, 18440–18448.

(11) Ghosh, S.; Keyvavina, S.; Van Roy, W.; Mizumoto, T.; Roelkens, G.; Baets, R. Ce:YIG/Silicon-on-Insulator waveguide optical isolator realized by adhesive bonding. *Opt. Express* **2012**, *20*, 1839–1848.

(12) Gilleo, M. A.; Geller, S. Magnetic and Crystallographic Properties of Substituted Yttrium-Iron Garnet, $3\text{Y}_2\text{O}_3 \cdot x\text{M}_2\text{O}_3 \cdot (5-x)\text{Fe}_2\text{O}_3$. *Phys. Rev.* **1958**, *110*, 73.

(13) Nahory, R. E.; Pollack, M. A.; Johnston, W. D., Jr.; Barns, R. L. Band gap versus composition and demonstration of Vegard's law for $\text{In}_{1-x}\text{Ga}_x\text{As}_y\text{P}_{1-y}$ lattice matched to InP. *Appl. Phys. Lett.* **1978**, *33*, 659–661.

(14) Saleh, B. E. A.; Teich, M. C. *Fundamentals of Photonics*, 2nd ed.; Wiley-Interscience: Weinheim, Germany, 1997.

(15) Soma, T.; Satoh, J.; Matsuo, H. Thermal expansion coefficient of GaAs and InP. *Solid State Commun.* **1982**, *42*, 889–892.

(16) Stadler, B.; Vaccaro, K.; Yip, P.; Lorenzo, J.; Li, Y.-Q.; Cherif, M. Integrated Magneto-Optical Materials and Isolators: A Review. *IEEE Trans. Magn.* **2002**, *38*, 1564.

(17) Gomi, M.; Tanida, T.; Abe, M. rf sputtering of highly Bi-substituted garnet films on glass substrates for magneto-optic memory. *J. Appl. Phys.* **1985**, *57*, 3888–3890.

(18) Yang, Q.-H.; Zhang, H.-W.; Wen, Q.-Y.; Liu, Y.-L. Effects of off-stoichiometry and density on the magnetic and magneto-optical properties of yttrium iron garnet films by magnetron sputtering method. *J. Appl. Phys.* **2010**, *108*, 073901.

(19) Yang, Q.; Huaiwu, Z.; Yingli, L.; Qiye, W. Effect of Post-Annealing on the Magnetic Properties of Bi:YIG Film by RF Magnetron Sputtering on Si Substrates. *IEEE Trans. Magn.* **2007**, *43*, 3652–3655.

(20) Sung, S.; Qi, X.; Stadler, B. J. H. Integrating yttrium iron garnet onto nongarnet substrates with faster deposition rates and high reliability. *Appl. Phys. Lett.* **2005**, *87*, 121111.

(21) Suzuki, T. Magnetic and magneto-optic properties of rapid thermally crystallized garnet films (invited). *J. Appl. Phys.* **1991**, *69*, 4756–4760.

(22) Vasiliev, M.; Wo, P. C.; Alameh, K.; Munroe, P.; Xie, Z.; Kotov, V. A.; Burkow, V. I. Microstructural characterization of sputtered garnet materials and all-garnet magnetic heterostructures: establishing the technology for magnetic photonic crystal fabrication. *J. Phys. D: Appl. Phys.* **2009**, *42*, 135003.

(23) Goto, T.; Eto, Y.; Kobayashi, K.; Haga, Y.; Inoue, M.; Ross, C. A. Vacuum annealed cerium-substituted yttrium iron garnet films on non-garnet substrates for integrated optical circuits. *J. Appl. Phys.* **2013**, *113*, 17A939.

(24) Goto, T.; Onbasli, M. C.; Kim, D. H.; Singh, V.; Inoue, M.; Kimerling, L. C.; Ross, C. A. A nonreciprocal racetrack resonator based

on vacuum-annealed magneto-optical cerium-substituted yttrium iron garnet. *Opt. Express* **2014**, *22*, 19047–19054.

(25) Block, A. D.; Dulal, P.; Stadler, B. J. H.; Seaton, N. C. A. Growth Parameters of Fully Crystallized YIG, Bi:YIG, and Ce:YIG Films With High Faraday Rotations. *IEEE Photonics J.* **2014**, *6*, 0600308.

(26) Boudiar, T.; Payet-Gervy, B.; Blanc-Mignon, M.-F.; Rousseau, J.-J.; Leberre, M.; Joisten, H.; Canut, B. Magneto-optical properties of yttrium iron garnet (YIG) thin films elaborated by radio frequency sputtering. *Proc. SPIE* **2004**, *5250*, 263.

(27) Leitenmeier, S.; Korner, T.; Griesbauer, J.; Herbort, M.; Heinrich, A.; Stritzker, B. Studies on the growth of epitaxial bismuth-substituted iron garnet on gadolinium gallium garnet single crystals by pulsed laser deposition. *J. Cryst. Growth* **2008**, *310*, 5392–5401.

(28) Sekhar, M. C.; Singh, M. R.; Basu, S.; Pinnepalli, S. Giant Faraday rotation in $\text{Bi}_{(x)}\text{Ce}_{(3-x)}\text{Fe}_5\text{O}_{12}$ epitaxial garnet films. *Opt. Express* **2012**, *20*, 9624–9639.

(29) Popova, E.; Keller, N.; Gendron, F.; Guyot, M.; Briando, M.-C.; Dumond, Y.; Tessier, M. Structure and magnetic properties of yttrium–iron–garnet thin films prepared by laser deposition. *J. Appl. Phys.* **2001**, *90*, 1422–1428.

(30) Eason, R., Ed. *Pulsed Laser Deposition of Thin Films: Applications-Led Growth of Functional Materials*; Wiley-Interscience: Hoboken, NJ, 2006.

(31) Huang, M.; Zhang, S.-Y. Growth and characterization of cerium-substituted yttrium iron garnet single crystals for magneto-optical applications. *Appl. Phys. A: Mater. Sci. Process.* **2002**, *74*, 177.

(32) Mino, S.; Tate, A.; Uno, T.; Shintaku, T.; Shibukawa, A. Properties of Ce-Substituted Yttrium Iron Garnet Film Containing Indium Prepared by RF-Sputtering. *Jpn. J. Appl. Phys.* **1993**, *32*, L994–L996.

(33) Enke, K.; Fleischhauer, J.; Gunßer, W.; Hansen, P.; Nomura, S.; Tolksdorf, W.; Winkler, G.; Wolfmeier, U. Part A: Garnets and Perovskites. In *Group III: Crystal and Solid State Physics*; Hellwege, K. H., Hellwege, A. M., Eds.; Landolt-Börnstein Numerical Data and Functional Relationships in Science and Technology New Series, Vol. 12; Hellwege, K. H., series Ed.; Springer-Verlag: Berlin Germany, 1978.

(34) Comstock, R. L.; Raymond, J. J. Magnetostriction of Ytterbium and Cerium in YIG. *J. Appl. Phys.* **1967**, *38*, 3737–3739.

(35) Belov, K. P.; Volkova, N. V.; Raitsis, V. I.; Ya Chervonenkis, A. Sov. Phys.—Solid State (Engl. Transl.) **1972**, *14*, 1607.

(36) Gibbons, D. F.; Chirba, V. G. Acoustical Loss and Young's Modulus of Yttrium Iron Garnet. *Phys. Rev.* **1958**, *110*, 770–771.

(37) MTI Corporation SiO_2 (single crystal quartz). <http://www.mtitl.com/sio2singlecrystalquartz.aspx> (accessed December 2014).

(38) Kozinski, J. A.; Gualtieri, J. G.; Ballato, A. Thermoelastic coefficients of alpha quartz. *IEEE Trans. Ultrason., Ferroelectr., Freq. Control* **1992**, *39*, 502–507.

(39) Shoji, Y.; Shirato, Y.; Mizumoto, T. Silicon Mach-Zehnder interferometer optical isolator having 8 nm bandwidth for over 20 dB isolation. *Jpn. J. Appl. Phys.* **2014**, *53*, 022202.

(40) Shoji, Y.; Mizumoto, T.; Yokoi, H.; Hsieh, I.; Osgood, R. M. Magneto-optical isolator with silicon waveguides fabricated by direct bonding. *Appl. Phys. Lett.* **2008**, *92*, 071117.

(41) Hu, J. *Planar Chalcogenide Glass Materials and Devices*, PhD Thesis, Massachusetts Institute of Technology, Cambridge, Massachusetts, 2009.